Earth Surf. Dynam., 3, 423–439, 2015
www.earth-surf-dynam.net/3/423/2015/
doi:10.5194/esurf-3-423-2015

Earth Surface Dynamics
Open Access

Denudation rates across the Pamir based on ^{10}Be concentrations in fluvial sediments: dominance of topographic over climatic factors

M. C. Fuchs[1,2], R. Gloaguen[1,2], S. Merchel[3], E. Pohl[1], V. A. Sulaymonova[1], C. Andermann[4], and G. Rugel[3]

[1]Remote Sensing Group, Institute of Geology, TU Bergakademie Freiberg, Bernhard-von-Cotta-Strasse 2, 09599 Freiberg, Germany
[2]Helmholtz-Zentrum Dresden-Rossendorf, Helmholtz Institute Freiberg for Resource Technology, Remote Sensing Group, Halsbrücker Strasse 34, 09599 Freiberg, Germany
[3]Helmholtz-Zentrum Dresden-Rossendorf, Helmholtz Institute Freiberg for Resource Technology, Bautzner Landstrasse 400, 01328 Dresden, Germany
[4]Section 5.1 Geomorphology, German Research Centre for Geoscience GFZ, Telegraphenberg, 14473 Potsdam, Germany

Correspondence to: M. C. Fuchs (fuchsm@mailserver.tu-freiberg.de)

Received: 17 November 2014 – Published in Earth Surf. Dynam. Discuss.: 29 January 2015
Revised: 17 June 2015 – Accepted: 17 July 2015 – Published: 24 August 2015

Abstract. A clear understanding of erosion processes is fundamental in order to comprehend the evolution of actively deforming mountain ranges. However, the relative contributions of tectonic and climatic factors and their feedbacks remain highly debated. In order to contribute to the debate, we quantify basin-wide denudation rates from cosmogenic ^{10}Be concentrations in modern river sediments in the Pamir. This mountain range is a unique natural laboratory because the ongoing India–Eurasia collision sustains high deformation rates and, on account of its position at the transition between Westerlies and monsoon, a strong regional climatic variability arises. Sample acquisition and preparation for accelerator mass spectrometry measurements were challenging due to difficult field accessibility, low quartz and high feldspar concentrations and crystal coating. Six samples along the main draining river, the Panj, and five samples within the major, east–west elongated tributary basins allow us to quantify basin-wide denudation rates for the first time in this orogen. An average denudation rate of $\sim 0.64\,\mathrm{mm\,yr^{-1}}$ reveals a rapid evolution of the entire Pamir. Denudation rates of tributary sub-basins highlight the strong contrast between the Pamir Plateau (0.05 to $0.16\,\mathrm{mm\,yr^{-1}}$) and its margins (0.54 to $1.45\,\mathrm{mm\,yr^{-1}}$). The intensity of denudation is primarily correlated with geometric properties of the surface, such as slope steepness (0.75 quartiles; R^2 of 0.81), and to a lesser extent to climatic factors such as precipitation. We thus argue that either tectonic uplift or base-level lowering are the main contributors to denudation processes. Multiple linear regression analysis (best R^2 of 0.93) suggests that precipitation may act as a limiting factor to denudation. The highest denudation rates coincide with areas of the northwestern Pamir margin that receive precipitation predominantly from the Westerlies during winter. There, the concentrated discharge during spring and early summer may sustain the pronounced denudation and allow the rapid sediment transport out of the basins. Low slope angles and dry conditions hamper the sediment flux on the plateau and, consequently, denudation. The magnitude of denudation in the Pamir is similar to rates determined in the southern Himalaya despite very different climatic and tectonic conditions. The discrepancy between rates of basin-wide denudation and the fluvial incision that is up to 10 times higher evidences a transient landscape in the Pamir. This underpins the hypothesis that river captures may have caused the strong base-level lowering that drives the enhanced incision of the Panj and its main tributaries.

Published by Copernicus Publications on behalf of the European Geosciences Union.

1 Introduction

The rapid evolution of active mountain chains depends on complex interactions between tectonically sustained rock uplift and climate-driven processes (see, e.g., Montgomery and Brandon, 2002; Burbank et al., 2003; Huntington et al., 2006; Godard et al., 2012, 2014). The variable in situ conditions imply spatial and temporal variations in erosion rates. Resulting patterns may allow us to constrain the role of tectonics and climate in mountain evolution and vice versa, for example, when erosion induces mass loss that will be compensated by isostatic rebound (see, e.g., Molnar and England, 1990; Burbank and Anderson, 2000; Champagnac et al., 2009). Available erosion data in the India–Asia orogenic belt are mainly concentrated on the southern escarpment of the Himalayas. Previous studies focussed on the coupling of tectonic uplift and the intensity of the Indian summer monsoon (ISM). The Pamir is drier and mainly influenced by the Westerlies that provide the bulk of precipitation during winter (and spring) in the form of snow (Pohl et al., 2015b, a). Short-term and/or small-scale erosion rates are not yet available for the Pamir. Quantitative estimates are needed to understand the role of differential tectonics and the climatic gradients in the magnitude of erosion as well as their variation depending on the captured time interval (see, e.g., Garzanti et al., 2007; Lupker et al., 2012). The comparison with other sites of the India–Asia collision zone may deliver new insights into the mechanisms of erosion in different climatic and tectonic settings. The tectonic and climatic setting of the Pamir provides ideal conditions to study erosion in response to variable drivers. First, the orogen lies at the westernmost part of the India–Asia collision zone, one of the Earth's largest and most rapidly deforming intracontinental convergence zones (see, e.g., Reigber et al., 2001; Mohadjer et al., 2010). Secondly, its position in the zone between the atmospheric circulation systems of the ISM and the Westerlies makes this region particularly interesting in order to study the role of different climatic conditions in mountain evolution. So far, the interaction of climatic and tectonic factors with the ongoing surface processes has not been explicitly assessed in the Pamir. Erosion rates have been analysed in the context of tectonic evolution (Stübner et al., 2013; Carrapa et al., 2014).

Stübner et al. (2013) inferred an erosion of roughly $0.5\,\mathrm{mm\,yr^{-1}}$ during the Miocene from thermochronological exhumation models and geometric reconstructions of the Shakhdara Dome. Carrapa et al. (2014) suggested a regional exhumation gradient of about $0.2\,\mathrm{mm\,yr^{-1}}$ in the northeastern Pamir and of between $0.6\,\mathrm{mm\,yr^{-1}}$ and above $2.0\,\mathrm{mm\,yr^{-1}}$ in the central and southern Pamir during the Miocene–Pliocene. They attribute the gradient to differing precipitation quantities that may cause much higher erosion rates in western marginal parts of the orogen. Such long-term and in some ways contradictory erosion rates inferred from exhumation reconstruction integrate climatic changes over several million years. They also cannot resolve the erosional response to climatic gradients or changes in uplift across the Pamir below the regional scale.

Variations in erosion were found to correlate with climate fluctuations that govern glacial processes (Gabet et al., 2008; Godard et al., 2012) and the intensity of the ISM (see, e.g., Bookhagen et al., 2005) in the Himalaya. The influence of precipitation on erosion also corresponds to regional relief characteristics that induce orographic effects (see, e.g., Garzanti et al., 2007; Gabet et al., 2008). Orographic rain shadow leads to a shift from precipitation- to temperature-sensitive erosion across the southern Himalayan escarpment. The shift results in an increased influence of concentrated peak discharge during the melting season on erosion (see, e.g., Burbank et al., 2012). Additionally, the availability of sediment (Burbank et al., 2012) and the magnitude-frequency distribution of direct runoff (Andermann et al., 2012) modulate rates of erosion. The generation of sediment and direct runoff are also thought to be genetically linked to tectonic and geometric factors. Slope or relief as a consequence of base-level lowering, hillslope thresholds or landslide frequency were found to correlate with erosion rates (see, e.g., Montgomery and Brandon, 2002; Ouimet et al., 2009). On the other hand, the correlation between erosion and long-term tectonic uplift in the Greater Himalaya is debated as denudation rates are suggested to adjust quickly to climatic variations (Burbank et al., 2003; Godard et al., 2014).

In this study, we aim at determining the magnitude of denudation in the Pamir on the timescale of 10^2 to 10^4 yr using ^{10}Be concentrations in the quartz of active river channel sediments. We analysed 11 samples of the Panj River network. The sampling sites were selected in order to cover the spatial variations in denudation rates within all major subbasins as well as changes with increasing basin sizes along the trunk river. The polymineral sediments required extensive preparation techniques to extract Be from pure quartz and to measure the long-lived cosmogenic radionuclide ^{10}Be by accelerator mass spectrometry at DREAMS (DREsden AMS, Helmholtz-Zentrum Dresden-Rossendorf, 6 MV, Cu cathode) (Akhmadaliev et al., 2013). Calculated production rates and shielding factors represent basins upstream of each sampling site. We tested geomorphic (altitude, relief, slope) and climatic (snow and ice cover and precipitation) basin parameters to explain the variations in basin-wide denudation rates using (multiple) linear regression analysis, and we discuss the influence of spatial and temporal averaging. This contribution focusses on the first denudation rates measured in the Pamir and their implications for our understanding of surface processes in that region. This paper complements previous works on OSL (optically stimulated luminescence) dating of river terraces and geomorphic indicators (Fuchs et al., 2013,

2014). Results showed the response of the Panj drainage system to tectonics, i.e. incision rate variability related to main tectonic structures in the Pamir and a possible reorganization of the Panj drainage system.

2 Regional setting

2.1 Geological setting

The Pamir is located at the northwestern end of the India–Asia collision zone. The series of sutures, magmatic belts and crustal blocks is assumed to consist of along-strike equivalents of the Tibetan Plateau that accreted to the Eurasian plate during the Paleozoic to Mesozoic (see, e.g., Burtman and Molnar, 1993; Schwab et al., 2004; Cowgill, 2010; Bershaw et al., 2012). The main tectonic structures allow us to distinguish three terranes: the northern, central and southern Pamir (Burtman and Molnar, 1993; Schwab et al., 2004). Cenozoic domes cover up to 30 % of the Pamir and comprise a steady-state elevated plateau (Ducea et al., 2003; Schwab et al., 2004; Schmidt et al., 2011; Stübner et al., 2013). The structural domes (Fig. 1a) expose Cretaceous arc-type granitoids, mantled by lower-grade to non-metamorphic rocks (Schwab et al., 2004; Robinson, 2009; Schmidt et al., 2011; Stübner et al., 2013). The northern Kurgovat Dome consists of high-grade metamorphosed Triassic rocks. The central Yazgulom, Sarez, Muskol and Shatput and the southern Shakhdara and Alichur domes expose high-grade metamorphic rocks of the Oligocene to Miocene ages with peak exhumation at ~ 15 Ma (Schmidt et al., 2011; Stübner et al., 2013).

The active frontal range of the Pamir curves nearly 180° from northern Afghanistan to western China (Bershaw et al., 2012). The northward propagation of the Indian plate induces east–west striking mountain ranges and governs neotectonic activity. Most of the seismicity occurs at the main Pamir Thrust (MPT), where the subduction beneath the frontal part of the orogen mainly accommodates crustal shortening (see, e.g., Koulakov and Sobolev, 2006; Schneider et al., 2013; Sippl et al., 2013). Recently published shortening rates reach 10–15 mm yr^{-1} across the MPT (Ischuk et al., 2013). The lateral margins of the orocline display a strike–slip motion of ~ 12 mm yr^{-1} along the western Darvaz Fault zone (DFZ) (Trifonov, 1978; Mohadjer et al., 2010) and < 1 mm yr^{-1} along the eastern Karakoram Fault zone (KFZ) (Strecker et al., 1995). The southern Pamir shear zone (SPSZ) delineates the boundary between the Pamir and the Hindu Kush to the south. This major east–west, low-angle normal fault comprises the southern boundary of the giant Shakhdara Dome. Plateau-internal neotectonic seismicity is related to the gravity-driven collapse of the plateau and the induced east–west extension and conjugated strike–slip (Fan et al., 1994; Strecker et al., 1995; Sippl et al., 2013)

2.2 Climatic setting

The position of the Pamir at the transition between the Westerlies and the ISM makes the region highly sensitive to variations in atmospheric circulation patterns. The Tropical Rainfall Measurement Mission (TRMM) spatial product 3B42 V7 (Huffman et al., 1997, 2007) reveals strong variations. Annual precipitation (mean 1998–2012) ranges from almost 0 to more than 500 mm in the Pamir (Fig. 1b). The Westerlies supply precipitation during winter and spring to the northwestern Pamir margins. The precipitation from the ISM to the south strongly decreases over the Hindu Kush and the Karakoram Range. The central Pamir receives very little annual precipitation, mainly in the form of snow. The westward increase in permanent snow and ice cover (Moderate Resolution Imaging Spectrometer, MCD12Q1, version 057, 2010; Strahler et al., 1999) illustrates the superimposition of concentrated precipitation at the Pamir margins and low temperature due to high altitudes (Fig. 1b).

Past fluctuations of glacial extents may affect erosion and sediment yields, when estimates integrate over longer time spans or when erosion products still reside in the basins. Glacial remnants on the Pamir Plateau attest to significant climatic variations during the late Quaternary. Their successively less extensive advances correspond to an increasing aridity in central Asia (Zech et al., 2005; Abramowski et al., 2006; Röhringer et al., 2012). Beryllium-10-based dating of moraines on the Pamir Plateau reveals that the most extensive glacial advance reached the inner-plateau valley floors 136–93 and 86–60 kyr ago, during Marine Isotope Stage (MIS) 4 or earlier, during MIS 5 to MIS 6. A potential ISM-driven MIS 3 advance is ambiguous due to the high scatter in ages of related hummocky moraines. Two less extensive advances are dated to 30–27 ka (MIS 3/MIS 2) and 24–22 ka (MIS 2). Younger glacial sediments are associated with deglaciation or minor readvances.

3 Material and methods

3.1 Beryllium-10-based modern denudation rates

Beryllium-10 concentrations in modern fluvial sediments are proportional to the time of rock surface exposure to interactions with cosmic rays and, consequently, inversely proportional to the rate of landscape lowering by weathering and physical erosion (von Blanckenburg, 2005; Dunai, 2010). The generally dry conditions in the Pamir (Fig. 1) suggest weathering to be of less importance in the total erosion budget. In this case, landscape lowering is dominated by the physical removal of material at the landscape's surface, which means that denudation rates become increasingly similar to erosion rates (see, e.g., Dunai, 2010). It may be convenient to use both terms interchangeably in the following and when comparing rates across timescales.

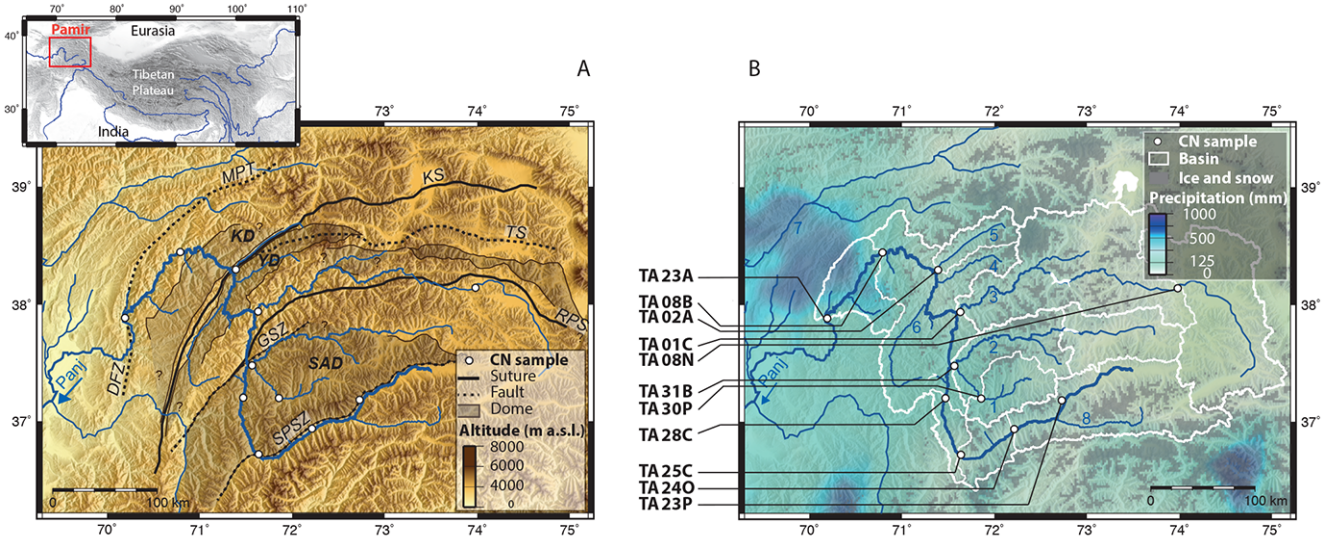

Figure 1. Regional setting of the Panj River system and sample locations (CN: cosmogenic nuclide; a.s.l.: above sea level). Panel (**a**): topography and main tectonic structures (DFZ: Darvaz Fault zone; MPT: main Pamir Thrust; KS: Kunlun suture; TS: Tanymas suture; RPS: Rushan-Psart suture; GSZ: Gunt shear zone; SPSZ: southern Pamir shear zone; KD: Kurgovat Dome; YD: Yazgulom Dome; SAD: Shakhdara and Alichur Dome; ASTER GDEM 30 m resolution, modified according to, e.g., Schwab et al., 2004; Stübner et al., 2013). Panel (**b**): sample locations along the Panj River network with related upstream drainage basins (tributaries represent the following: 1 – Shakhdara; 2 – Gunt; 3 – Bartang; 4 – Yazgulom; 5 – Vanj; 6 – Shiva; 7 – Vakhsh; 8 – Wakhan). The climate is shown by the distribution of annual precipitation (TRMM 3B42 V7, 1998–2012; Huffman et al., 1997, 2007) and permanent snow and ice cover (MODIS MCD12Q1; Strahler et al., 1999, data for the year 2010).

The inverse proportionality of ^{10}Be concentration C in quartz and denudation rate ε (Lal, 1991; Brown et al., 1995; von Blanckenburg, 2005) can be described by

$$\varepsilon = \left(\frac{P}{C} - \lambda\right) \times z^*, \quad (1)$$

where λ is the decay constant of the nuclide and P its production rate. To calculate λ by

$$\lambda = \frac{\ln(2)}{t_{1/2}}, \quad (2)$$

we used the ^{10}Be half-life ($t_{1/2}$) of 1.387 ± 0.012 Myr (Korschinek et al., 2010). For the attenuation depth z^*, we used 60 cm to represent silicate rocks (Lal, 1991; von Blanckenburg, 2005). For constant ^{10}Be production and material removal at the surface, the measured nuclide concentration represents the time material residing within z^*. Hence, estimates averaged over the time (T_{ave}) are needed to remove the "cosmogenic memory" that material acquires within z^*. (Brown et al., 1995; Bierman and Steig, 1996; von Blanckenburg, 2005; Dunai, 2010). For further details see the Supplement.

3.2 Sampling strategy

We sampled 11 locations of the Panj River network (Fig. 1b). Five sampling sites represent the increasing basin along the trunk river reach until the Panj crosses the DFZ. Three major tributaries (Gunt, Bartang and Vanj rivers; Fig. 1b) were sampled near their confluence with the Panj and three additional sites were selected to represent upstream sub-basins. This relatively low number of samples is explained by the fairly difficult accessibility of the region. Additionally, difficulties in finding suitable sites of modern fluvial sediments arose from the high stream power of the Panj that limits the deposition of sand in the Pamir.

We chose locations before confluences as far as possible from upstream tributaries. This ensured a complete mixing of sediment grains that represent all upstream source areas. Locations where slope failure or fan sedimentation from minor tributaries indicated local perturbations have been avoided. We sampled the uppermost 1–3 cm of the sediment in the active river channel. All samples consisted of predominantly sand-sized, polymineral material.

Thus, we collected 3–5 kg of fluvial sediment per sample to retrieve sufficient quantities of quartz for Be extraction and subsequent ^{10}Be AMS (accelerator mass spectrometry) measurements.

3.3 Sample preparation and ^{10}Be measurements

The polymineral sediment samples required the enrichment of quartz before starting chemical cleaning and Be extraction because of relatively low quartz but high feldspar con-

tents (up to 50 %) as well as mineral coatings. Quartz enrichment included wet sieving (with a focus on 250–500 µm; for samples TA28C and TA30P only the coarser fraction 500–1000 µm yielded sufficient material), magnetic separation and an ultrasonic bath. Up to six cycles of quartz cleaning with a 1 : 1 solution of HCl (32 %) and H_2SiF_6 (34 %) (Brown et al., 1991) were insufficient to diminish the feldspar. Feldspar may cause bias in quartz results because of its differing rate of ^{10}Be production, lower chemical resistance and high aluminium contents that affect chemical procedures. Therefore, we introduced a feldspar flotation to separate pure quartz (Herber, 1969). The feldspar flotation was carried out in a solution of 0.2 % HF with a pH of 2.4–2.7. The foam agent dodecylamine supported the adherence of feldspar to bubbles pumped into the flotation cell.

Atmospheric ^{10}Be was removed by dissolving 30 % of the extracted quartz fraction with 48 % HF during three cycles. The BeO separation and Be extraction followed the procedures by Merchel and Herpers (1999) (for details, see the Supplement). We added about 300 µg of a ^{9}Be carrier (Phena DD, $(3.025 \pm 0.009) \times 10^{-3}$ ^{9}Be g^{-1}; Merchel et al., 2008).

Adding Nb (6 times the dry oxide weight) finalized the target preparation. AMS measurements were conducted at DREAMS (Helmholtz-Zentrum Dresden-Rossendorf, 6 MV, Cu cathode) using the in-house standard SMD-Be-12 (Akhmadaliev et al., 2013) normalized against the NIST SRM 4325 standard (^{10}Be / ^{9}Be ratio of $(2.79 \pm 0.03) \times 10^{-11}$; Nishiizumi et al., 2007). A round-robin exercise of AMS facilities confirmed robust standard calibration and measurement configuration (Merchel et al., 2012). Processing blanks were treated and measured parallel to the sediment samples. We subtracted the blank isotope ratios in the range of 0.3–1.7 % (^{10}Be / ^{9}Be ratio of 2.0×10^{-15} and 2.1×10^{-15}) from the measured ratios of all samples.

3.4 Production rates and shielding factor

We calculated ^{10}Be production rates and shielding for the studied sites by scaling the reference sea level and high-latitude (SLHL) production rate of 4.5 at g^{-1} quartz yr^{-1} (cf. Balco et al., 2008), according to Stone (2000). Representative estimates need to account for the variable hypsometry of the whole basin upstream of the sampled site. We identified the upstream area for each sampling site using a ASTER GDEM (Advanced Spaceborne Thermal Emission and Reflection radiometer global digital elevation model, 30 m resolution, NASA Land Processes Distributed Active Archive Center) and calculated raster-cell-resolved production rates and shielding factors (for details see the Supplement). Assuming total shielding by permanent ice and snow cover, the production of ^{10}Be will only take place in areas that are actually exposed to the cosmic ray flux. Consequently, we excluded snow- and ice-covered areas from our calculations of ^{10}Be production rates. The areas of permanent snow and ice cover are based on MODIS (Moderate Resolution Imaging Spectrometer) land cover type data MCD12Q1 (Strahler et al., 1999) and the classification scheme according to the IGBP (International Geosphere Biosphere Programme). The available data covers the years 2000–2012. For our calculations, we use the year 2010, which is among those with the most extensive snow and ice cover.

Variations in permanent snow and ice cover during the last millennia are unknown. Palaeorecords only give information on glacier extents on longer timescales and do not include the distribution of snow cover nor do MODIS data distinguish between snow and ice. Hence, the MODIS data from 2010 may underestimate the snow and ice cover during the last millennium. Nevertheless, we assume only low variations because glacier extents have already largely retreated since the Last Glacial Maximum, corresponding to an increasing aridity (see, e.g., Zech et al., 2005; Abramowski et al., 2006; Röhringer et al., 2012). Ongoing glacial retreat is indicated for the last roughly 50 years (Aizen, 2011; Gardelle et al., 2013). The area upstream of Lake Yashilkul was not included in basin analyses as a large landslide has dammed the plateau discharge and sediment flux for several 10^4 years (Zech et al., 2005; Brookfield, 2008).

We corrected production rate estimates by topographic shielding. Shielding factors for each GDEM raster cell refer to the horizon line within a 10 km distance according to the method of Codilean (2006). Norton and Vanacker (2009) found only a low underestimation of shielding when using a DEM (digital elevation model) of 30 m resolution in steep terrain. Other sources are considered negligible as snow- and ice-covered areas are already excluded from production rate calculation and vegetation is scarce due to the dry climate and high basin altitudes.

The raster-cell-resolved production rates and shielding factors show non-normal distributions skewed to polymodal according to the basin topography. We used the arithmetic mean and calculated uncertainties based on the standard deviation to account for the high value variability within basins. The uncertainties of denudation rates represent the sum of the AMS measurement error of the ^{10}Be concentration and the calculated uncertainties of production rates and shielding.

3.5 Sample basin parameters

Basin-wide denudation rates have been found to correlate with altitude, slope, relief, precipitation and glaciated area (see, e.g., Schaller et al., 2001; Montgomery and Brandon, 2002; von Blanckenburg, 2005; Norton et al., 2010). We use topographic and climatic basin parameters to examine the influence of these factors on denudation rates. We describe the variability of parameters within the sampled basins by probability density estimates, using the GDEM and the R programming environment (R Core Team, 2013). Apart from altitude and slope, we calculate the relief of each basin to characterize the altitude range on different scales. The basin relief

refers to the total difference between the 0.75 and 0.25 quartiles of basin altitudes. The use of quartiles compensates for the bias towards highest relief for the largest basins. The local relief represents the altitude range normalized to a given area. We used moving windows of 1 and 4 km width to determine the relief from the GDEM. A smaller window size narrows relief estimates down to slope, a wider window size reproduces trends in basin relief. Precipitation estimates refer to the TRMM product 3B42 V7 (Huffman et al., 1997, 2007) of the years 1998–2012. In addition, we estimate the snow- and ice-covered area to be proportional to the basin size using the MODIS data of the year 2010 (see above, Strahler et al., 1999).

The median and 0.25 and 0.75 quartiles of each parameter were used for (multiple) linear regression analyses. We thus expect to discriminate between the potential topographic and climatic parameters that can explain the variance in denudation. The use of quartiles allows us to test the relevance of the general condition within a basin and to evaluate the influence of low or high values of individual parameters. Linear regression analyses represent a standard tool for a simple, straightforward evaluation of basin characteristics. Sensu stricto, correlation analyses based on linear regression are designed for normally distributed data. We used the robust linear regression model available in the R environment (R Core Team, 2013) to account for the small data set and reduce the relevance of any extreme values that skew the data. We employ the coefficient of determination (R^2) as a quantitative indicator of basin parameters that likely explain the variance in denudation rates. This enables us to compare results to relations found in other mountain regions. We do not rank the variables. The regression is meant to test which of the relief descriptors or climatic indicators describe the variable denudation rate better.

4 Results

4.1 Sample basin properties

The Panj River network is strongly asymmetric. The trunk reach connects tributary outlets from south to north close to the western drainage divide. Basins of the southern Panj and of the major Panj tributaries show preferential east–west lengthened shapes (Fig. 1b). The parallel configuration of the major basins allows us to resolve south–north changes in factors controlling denudation. The lengthened basins of the Gunt and Bartang rivers (TA31B and TA01C) integrate over gradients between the Pamir Plateau and its western margin. The Shakhdara (TA30P) and Murghab rivers (TA08N) allow us to elucidate the conditions in upstream areas related to the Pamir Plateau, while the Vanj River basin (TA02A) does not include any plateau-related basin sections and solely represents marginal conditions.

The median basin altitudes slightly decrease from 4800 to 4200 m a.s.l. along the course of the Panj (cf. Fig. 1). The minimum altitudes represent the fluvial levels and illustrate the downstream (northward) increase in the total altitude range. Base levels drop from 3600 m to 700 m a.s.l. (Table 1), while maximum altitudes remain more or less constant. This strong decrease in minimum altitudes is evidence of the strong fluvial incision of the Pamir margins. On the plateau, altitudes cluster between 3800 and 5000 m a.s.l., with significantly less frequent lower altitudes (Fig. 2a, bottom). The basins of the southern Panj are slightly higher compared to those at the western Pamir margin. A strong drop in altitude frequencies delineates the Pamir Plateau from its margins (Fig. 2a). The main frequency contrast occurs at ∼ 3800 m a.s.l. at the southern Pamir margin and less sharply at ∼ 3600 m a.s.l. at the western margin. Two minor peaks at ∼ 3300 m a.s.l. and ∼ 2800 m a.s.l. indicate local base levels below the Pamir Plateau (cf. Fig. 2a, top) in the southern Panj basins. The local base levels are masked by the increasing basin size in the western Pamir basins. The Vanj Basin (TA02A) stands out due to the absence of the marked altitude frequency drop, indicating the predominance of margin-related altitudes and low influences of plateau conditions.

The relative proportions of slopes within basins correspond to the respective altitude distributions. Highly variable slopes display strongly bimodal distributions, where east–west elongated basins range over plateau and marginal basin sections (Fig. 2b, middle). The narrow peak of slope frequencies below 5° scales with the plateau-related, very flat basin sections between 4000 m and 5000 m a.s.l. (cf. upper Bartang, TA08N, Fig. 2b, bottom). Such areas are less extensive in the southern Panj basins that delineate the Pamir at its southern margin (Fig. 2b, top). The second, much broader frequency peak shows a hillslope cluster at roughly 35°. The Vanj Basin (TA02A, Fig. 2, centre) stands out with a negatively skewed slope distribution and maximum frequencies at ∼ 40°. Although the Shakhdara Basin (TA30P, Fig. 2b, bottom) drains the plateau, it lacks the low slope frequency peak. The slope distribution is broad with a plateau of high frequencies between 10 and 30°. This suggests a transient basin position at the edge of the Pamir Plateau.

Areas of permanent ice and snow cover reflect the predominant moisture supply from the northwest and south, while the central-eastern parts of the Pamir remain arid (Fig. 1b). The coverage of snow and ice is very heterogeneous in the Pamir basins. Two basins show a large coverage of permanent ice and snow. The highest value (55 %) of a small basin of the upper Panj tributary (TA23P) corresponds to high altitudes between 4500 m and 5500 m a.s.l., while the northernmost basin of the Vanj River (TA02A, 37 %) lies much lower but receives increased orographic precipitation from the Westerlies (cf. Fig. 2c, middle). In contrast, only 5 % of the upper Bartang Basin (TA08N) at the eastern plateau is permanently covered by snow and ice (Table 1). A similar picture can be drawn from the median of TRMM-based mean annual precipitation (1998–2012). The largest

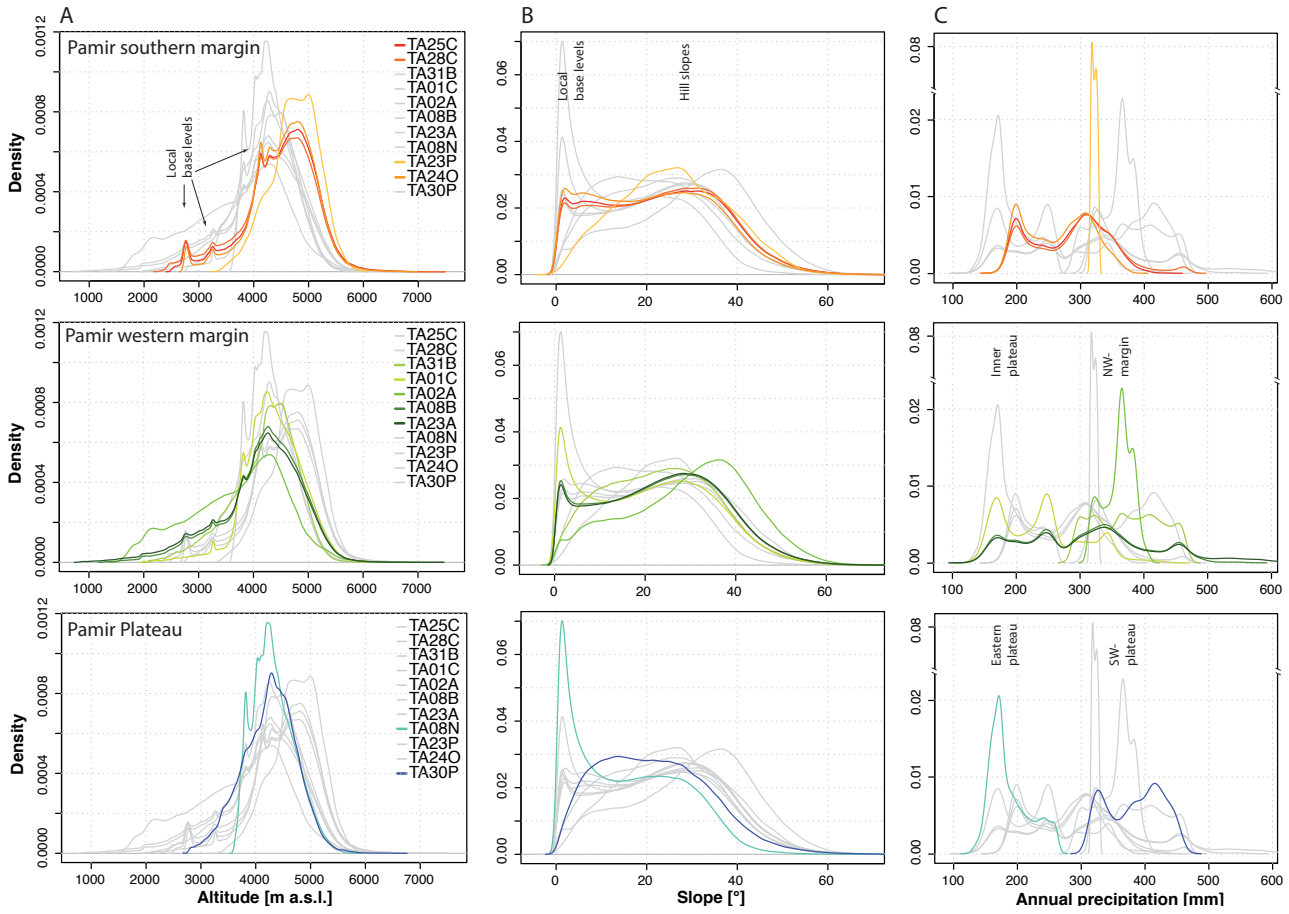

Figure 2. Frequency distributions of altitude **(a)**, slope **(b)** and precipitation **(c)** for individual sample basins, grouped due to their location at the southern or western margin of the Pamir or at the Pamir Plateau. Relative frequencies of altitude and slope were calculated from an ASTER GDEM of 30 m resolution and precipitation from the TRMM product 3B42 V7 (Huffman et al., 1997, 2007) (names of basins are the same as the sample names in Fig. 1 and Table 1).

basins, TA23A and TA08B, indicate a regional average of $\sim 300\,\mathrm{mm\,yr^{-1}}$. Variations in precipitation are mainly controlled by orographic gradients of the predominant atmospheric circulations.

4.2 Denudation rate parameters

The ^{10}Be concentrations vary significantly between the sampled basins (Table 2). Nuclide concentrations (5.7–$7.6 \times 10^4\,\mathrm{at\,g^{-1}}$) along the Panj do not show any trend from smaller upstream basins towards downstream basins of increasing size. The tributary basins display a northward decrease in concentrations (TA31B, TA01C, TA02A), but the estimates represent averages over differing sections of plateau-related and marginal basin areas. In particular, concentrations measured for the Bartang Basin (TA01C) also integrate the upstream basin (TA08N) with the highest ^{10}Be concentrations of $(98.5 \pm 2.1) \times 10^4\,\mathrm{at\,g^{-1}}$, while the marginal basin section likely contributes only very low concentrations to the sediment mix. Similarly, the Gunt Basin (TA31B) comprises also the Shakhdara River subbasin (TA30P) that has twice the concentration found in the entire Gunt Basin. The Vanj Basin (TA02A) yields the lowest concentration with $(1.9 \pm 0.1) \times 10^4\,\mathrm{at\,g^{-1}}$, without any contribution from plateau-related upstream basin section.

Estimated production rates of ^{10}Be (cf. ^{10}Be production rates due to neutrons in Fig. S1, top, in the Supplement) correspond to the basin topography (cf. Fig. 2a) with one prominent maximum at $\sim 80\,\mathrm{at\,g^{-1}\,yr^{-1}}$. The increased altitude range at the western Pamir margin causes skewed distributions. Topographic shielding factors range from roughly 0.8 to 1.0, with a narrow and a wide maximum in frequencies (Fig. S1, bottom). The frequencies mimic the distribution of slope angles (cf. Fig. 2b). Excluding areas covered by snow and ice lowers the production rates in a systematic manner, modulated by the amount of precipitation (Fig. S2a). Not excluding the ice- and snow-covered areas would result in erroneously high production rates. The highest basin sections theoretically should have high production rates, but actually no ^{10}Be is produced. Such overestimated production rates

Table 1. Details on sampling sites and related upstream drainage area (sample basin). Ice: permanent ice and snow cover, based on the year 2010 from MODIS MCD12Q1 (Strahler et al., 1999); the uncertainty given represents the standard deviation of MODIS MCD12Q1 between 1998 and 2012. Altitude, slope and precipitation represent the median of the value distribution within sampled basins (see Fig. 2) calculated from the ASTER GDEM (30 m resolution). The rainfall data reflect the annual mean precipitation, based on the Tropical Rainfall Measuring Mission (TRMM) product 3B42 V7, 1998–2012 (Huffman et al., 1997, 2007). Bold letters in sample names indicate notations used in the text and figures.

Sample	River	Location			Sample basin				
		Long (°E)	Lat (°N)	Altitude (m a.s.l.)	Area (km^2)	Ice (%)	Altitude (m a.s.l.)	Slope (°)	TRMM ($mm\,yr^{-1}$)
Panj:									
TA0909**23A**	Panj	70.177	37.901	731	71727	16.3 ± 2.9	4213	24.3	316
TA0909**08B**	Panj	70.787	38.456	1220	67749	17.1 ± 3.0	4255	24.1	309
Vanj:									
TA0909**02A**	Vanj	71.378	38.293	1551	2079	37.0 ± 6.5	3869	31.4	364
Bartang:									
TA0909**01C**	Bartang	71.610	37.490	2030	29243	13.6 ± 2.4	4351	21.4	239
TA1108**08N**	Aksu	73.965	38.161	3603	13548	4.0 ± 0.7	4283	14.5	176
Gunt:									
TA0908**31B**	Gunt	71.527	37.490	2078	8437	18.7 ± 3.3	4294	23.3	376
TA1108**30P**	Shakhdara	71.845	37.210	2785	3507	13.5 ± 2.4	4281	20.8	390
Southern Panj:									
TA0908**28C**	Panj	71.460	37.220	2275	15230	26.1 ± 4.6	4519	23.8	298
TA0908**25C**	Panj	71.596	36.730	2491	13625	28.2 ± 4.9	4574	23.2	290
TA1108**24O**	Panj	72.206	36.929	2754	11064	29.2 ± 5.1	4591	21.6	272
TA1108**23P**	(Pamir)	72.737	37.173	3552	84	55.1 ± 9.6	4770	25.6	321

would suggest a shorter time span for the acquisition of the sediment's nuclide concentration. Excluding snow- and ice-covered areas produced representative production rates for the areas exposed to cosmic ray flux (Fig. S2a). The limited snow and ice coverage on the eastern plateau affects production rates less compared to the rates in the marginal basins of the northwestern Pamir. The change in denudation rates amounts to less than 10 % for all sampled basins, except for TA23P and TA02A, which have values up to 20 % lower (see the Supplement for details on the parameters for denudation rate calculation, including snow- and ice-covered areas, and shielding-corrected production rate).

4.3 Basin-wide denudation rates

The two largest basins (TA23A and TA08B) reveal a high average denudation for the entire Pamir, with rates of $\sim 0.64\,mm\,yr^{-1}$ (Fig. 3). Denudation rates determined along the Panj resemble the average conditions and stay relatively consistent despite significant changes in basin sizes. Southern Panj basins indicate a slight westward decrease in denudation with increasing basin size. A denudation rate of $0.79 \pm 0.19\,mm\,yr^{-1}$ for the eastern, upper Panj (TA23P, small Pamir River tributary) decreases to $0.58 \pm 0.18\,mm\,yr^{-1}$ for the entire southern Panj Basin before the river course deflects to the north. Denudation rates rapidly increase downstream to $0.74 \pm 0.24\,mm\,yr^{-1}$, despite the relatively modest growth of drainage area (~ 13 %).

The basin-wide rates of the major Panj tributaries (Gunt, Bartang, Vanj) reveal strong contrasts in denudation across the Pamir, ranging from $0.05 \pm 0.01\,mm\,yr^{-1}$ to $1.45 \pm 0.56\,mm\,yr^{-1}$ (Table 2). The differences evidence an increase in denudation from the southeastern central plateau towards the northwestern margins. Two upstream sub-basins determine low denudation on the Pamir Plateau with $0.05 \pm 0.01\,mm\,yr^{-1}$ for the easternmost inner plateau (TA08N) and $0.16 \pm 0.05\,mm\,yr^{-1}$ for the southwestern Shakhdara Basin (TA30P). The morphometry of those plateau-related areas is characterized by the predominance of altitudes above 3600 m a.s.l. and large areas of slopes below 5° (cf. Table 2). Denudation rates determined immediately before the confluence with the Panj show a northward increase from ~ 0.37 to $1.45\,mm\,yr^{-1}$ in major tributary basins (Gunt, Bartang, Vanj). Rates in the elongated Gunt (TA31B) and Bartang (TA01C) basins integrate the low denudation of upstream plateau-related sub-basins (TA08N and TA30P). Consequently, we assume an intensified denudation in the downstream, marginal basin sections compared to the basin-wide average determined here. This assumption fits the denudation rate of $1.45 \pm 0.56\,mm\,yr^{-1}$ for the Vanj Basin (TA02A). This basin reflects the conditions at the northwestern Pamir margin without significant sections of plateau-related areas.

We estimate the denudation rates of the lower sections of the Gunt (GUNT) and the Bartang (BARlow) based on the measured data we have for the entire basin and its upstream

Table 2. Parameters and results of denudation rate calculation. AMS measurements were performed at DREAMS, Helmholtz-Zentrum Dresden-Rossendorf. The ^{10}Be concentrations are corrected for processing blanks (^{10}Be / ^{9}Be ratios of 2.0×10^{-15} and 2.1×10^{-15}, i.e. 0.3–1.7 % of the sample values). The effective production rate represents the sum of the neutron- and muon-induced (fast and stopped muons) production of ^{10}Be in quartz (P_{sum}), calculated using the scaling system of Stone (2000) and corrected for topographic shielding using the method of Codilean (2006). The values for individual basins are based on the arithmetic mean. T_{ave} gives the average time needed to erode the typical attenuation depth of ~ 60 cm as a proxy of "cosmogenic memory", describing the time over which the cosmogenic nuclide inventory averages. Bold letters in sample names indicate notations used in the text and figures.

Sample	AMS ^{10}Be conc. ($\times 10^4$ at g^{-1})	Production rate P_{sum} (at g^{-1} yr^{-1})	Shielding (factor)	Denudation rate (mm yr^{-1})	T_{ave} (yr)
Panj:					
TA090**23A**	5.7 ± 0.2	70.5 ± 17.3	0.92 ± 0.06	$\mathbf{0.68 \pm 0.23}$	880
TA090**08B**	6.7 ± 0.2	72.4 ± 17.3	0.92 ± 0.06	$\mathbf{0.59 \pm 0.20}$	1010
Vanj:					
TA090**02A**	1.9 ± 0.1	52.0 ± 13.3	0.87 ± 0.06	$\mathbf{1.45 \pm 0.56}$	410
Bartang:					
TA090**01C**	5.3 ± 0.2	79.5 ± 12.8	0.93 ± 0.06	$\mathbf{0.83 \pm 0.22}$	720
TA110**08N**	98.5 ± 2.1	80.2 ± 11.0	0.95 ± 0.04	$\mathbf{0.05 \pm 0.01}$	13010
Gunt:					
TA090**31B**	11.1 ± 0.4	73.1 ± 13.6	0.92 ± 0.06	$\mathbf{0.37 \pm 0.11}$	1640
TA110**30P**	25.5 ± 1.5	75.4 ± 12.0	0.93 ± 0.06	$\mathbf{0.16 \pm 0.05}$	3650
Southern Panj:					
TA090**28C**	5.9 ± 0.3	78.3 ± 16.5	0.92 ± 0.06	$\mathbf{0.74 \pm 0.24}$	810
TA090**25C**	7.6 ± 0.3	80.4 ± 16.4	0.92 ± 0.06	$\mathbf{0.58 \pm 0.18}$	1030
TA110**24O**	6.3 ± 0.6	81.7 ± 14.2	0.93 ± 0.06	$\mathbf{0.72 \pm 0.24}$	830
TA110**23P**	5.7 ± 0.2	84.7 ± 11.1	0.89 ± 0.06	$\mathbf{0.79 \pm 0.19}$	760

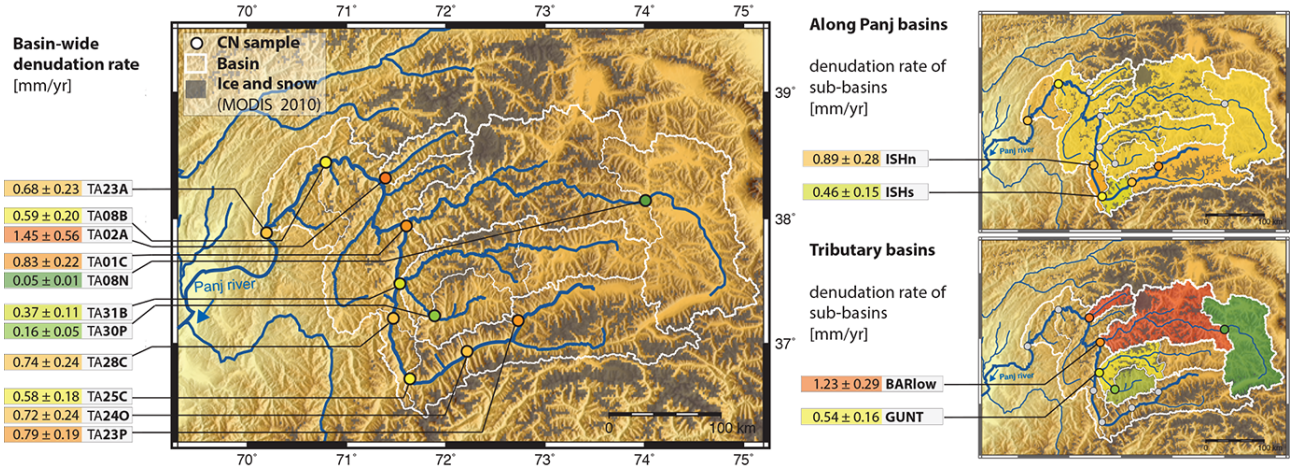

Figure 3. Basin-wide denudation rates of along Panj and major tributary samples (CN: cosmogenic nuclide; colour code represents magnitude of denudation with green for low and red for high rates). Calculations based upon AMS measurements of ^{10}Be concentrations in modern fluvial sediments and GDEM processing for production rates and topographic shielding. Denudation rates of the sub-basins ISHn, ISHs, BARlow and GUNT represent slope-weighted estimates inferred from sampled basins (corresponding up- and downstream basins) and using derived measurement results from Eq. 3 (for details see text and Table 3).

basin section. We scaled the denudation rates proportionally to their relative area using a simple approximation. Accordingly, the denudation rate of the entire basin (ε_{total}) represents the sum of the area-weighted denudation rates in the upper and lower sub-basins (up and down).

$$\varepsilon_{total} = a \times \varepsilon_{up} + (1 - a) \times \varepsilon_{down} \quad (3)$$

The area factor a (normalized to 1) describes the section of the upstream sub-basin relative to the area of the entire

basin. This area-weighted approach assigns denudation rates of 0.53 mm yr^{-1} (GUNT) and 1.64 mm yr^{-1} (BARlow) to corresponding downstream basin sections (ε_{down}; Table 3). Applying the same approach to the southern Panj basins enhances the contrast in denudation where the southern Panj deflects to the north at the western Pamir margin. Using the rates from basin TA24O and TA25C results in an area-weighted denudation of only 0.02 mm yr^{-1} for the inferred sub-basin ISHs. In contrast, the area weighting leads to a very high denudation rate of 1.81 mm yr^{-1} for the inferred sub-basin between TA25C and TA28C (ISHn). This high value may be compared to those of the lower Bartang Basin (BARlow) and the Vanj Basin (TA02A). However, the area-weighted denudation rates do not necessarily represent the actual contribution of individual basin sections to the sampled mix of material.

The area factor a can be replaced by a slope factor s to account for morphometric differences in basin sections. The factor s describes the ratio of the sub-basin slope scaled to the slope of the entire basin and normalized to 1 (i.e. division by 2 in the case of two sub-basins). Slope-weighted denudation rates are then determined by using Eq. 3. Inferred rates indicate an improved fit to morphometric units and to observed trends in the measured basin-wide rates. The slope-weighted denudation rates are 0.54 mm yr^{-1} for the sub-basin GUNT, 1.23 mm yr^{-1} for BARlow, 0.46 mm yr^{-1} for ISHs and 0.89 mm yr^{-1} for ISHn (Table 3).

4.4 Relationship between denudation rates and basin parameters

The absence of any trend with increasing basin size suggests no significant nuclide acquisition during grain transit through the basin. Results reveal a primary role of topographic basin parameters in variations in denudation rates (Fig. 4).

The relationship applies to measures of altitude differences (relief) within a given area. The goodness of fit strongly depends on scale, i.e. the reference area used to quantify the relief. The basin relief (BR, Fig. 4a) is not suited to explain rates of denudation, while the local relief (LR, Fig. 4a) yields an R^2 of 0.68 when being estimated within 1 km. The highest correlation with denudation rates is attained with basin slope values. The correlation with median slopes yields an R^2 of 0.73. The correlation with the steepest slopes of a basin seems to be even more important as the 0.75 quartiles of basin slopes explain denudation rates with an R^2 of 0.81 (Fig. 4b). The correlation of denudation with slopes suggests that the slope-weighted denudation rate estimations for the inferred sub-basins GUNT, BARlow, ISHs and ISHn fit in with the primary relationship found in regression analyses (Table 3).

The only slight variations in mean annual precipitation between 270 and 380 mm (based on TRMM data) cannot explain the pattern of denudation (R^2 of < 0.1). Similar denudation rates cluster regardless of relatively low or high precipitation. The only relation found is that all basins with the highest denudation rates receive the highest amounts of annual precipitation. The limited influence of precipitation on denudation may originate from the overall low precipitation, predominantly in the form of snow. The accumulated winter precipitation causes a temperature-sensitive delayed release with peak discharge during the melting season. The relative area covered by snow and ice shows no strong relation to denudation rates (R^2 of < 0.4).

We performed a multiple linear regression analysis with two predictors for denudation to test for additive effects. Other regression models are possible but inappropriate for the small data set and less comparable to any linear relations found in the one predictor linear regression analysis. The multiple linear regression addresses the question of whether any predictor requires preconditions to become effective. Including more components resulted in multicollinearity and insignificant effects on the goodness of correlation. The best results were obtained by combining the 0.75 quartiles of slope and TRMM precipitation data. The R^2 of 0.93 (Fig. 4c) suggests a good fit of the additive linear model. Other two predictor combinations yielded lower R^2 values compared to the one predictor linear regression using slope angles. The regression with slope gradient and TRMM rainfall data indicates that low slopes imply low denudation despite variations in precipitation, while high precipitation contributes to high denudation rates in the case of steep slopes.

5 Discussion

5.1 Averaging times of Pamir denudation rates

For a robust interpretation of the Pamir denudation rates, it is important to consider the scales of averaging in terms of time and space.

The denudation rates in the Pamir are averaged over timescales of 10^2 to 10^4 years, i.e. the Holocene (Table 2). The high denudation rates of most Pamir basins imply a T_{ave} of less than 10^3 years. This fast renewal of the nuclide inventory suggests that the denudation rates represent modern conditions. Although the climate likely underwent fluctuations, there is no evidence for major changes during that time in glacial records (Zech et al., 2005; Abramowski et al., 2006; Röhringer et al., 2012). The moderate denudation rates (about 0.16–0.37 mm yr^{-1}) calculated for the Gunt (TA31B) and the Shakhdara basins (TA30P) are averaged over the time since the middle to late Holocene. Only the eastern Pamir Plateau basin (TA08N) has a significantly longer T_{ave}. The derived denudation rate averages over the time since the MIS 2–MIS 1 transition (Table 2) and, hence, integrates over the Holocene deglaciation period. However, the large areas of low slopes and flat, sediment-filled valleys of the inner Pamir are indicative of low denudation, persistent over long timescales. Additionally, influences of short-term environmental fluctuations on denudation rates decrease with

Table 3. Approximated denudation rates of sub-basins using weighting factors that account for basin area (a) and basin slope (s). The weighting factors a and s are applied to determine variations in denudation within large basins when the rates are known (determined based on measured ^{10}Be concentrations and corresponding production rates) for the entire basin and one of its sub-basins (ε: denudation rate; total: sample data for entire basin; up: sample data for upper sub-basin; down: inferred rate for lower sub-basin using the area or slope-based weighting factors; a: area factor describing the proportion of the respective sub-basin normalized to 1; s: slope factor describing the slope variations in sub-basins normalized to 1).

Basin	Basin label	Denudation rate (mm yr^{-1})				Basin area		Basin slope	
		ε_{total}	ε_{up}	$\varepsilon_{down(area)}$	$\varepsilon_{down(slope)}$	a_{up}	a_{down}	s_{up}	s_{down}
Gunt	GUNT	0.37 ± 0.11	0.16 ± 0.05	0.53 ± 0.16	0.54 ± 0.16	0.44	0.56	0.45	0.55
Bartang	BARlow	0.83 ± 0.22	0.05 ± 0.01	1.64 ± 0.38	1.23 ± 0.29	0.51	0.49	0.34	0.66
Southern (TA25C)	Panj ISHs	0.58 ± 0.18	0.72 ± 0.24	0.02 ± 0.01	0.46 ± 0.15	0.80	0.20	0.47	0.53
Southern (TA28C)	Panj ISHn	0.74 ± 0.24	0.58 ± 0.18	1.81 ± 0.57	0.89 ± 0.28	0.87	0.13	0.49	0.51

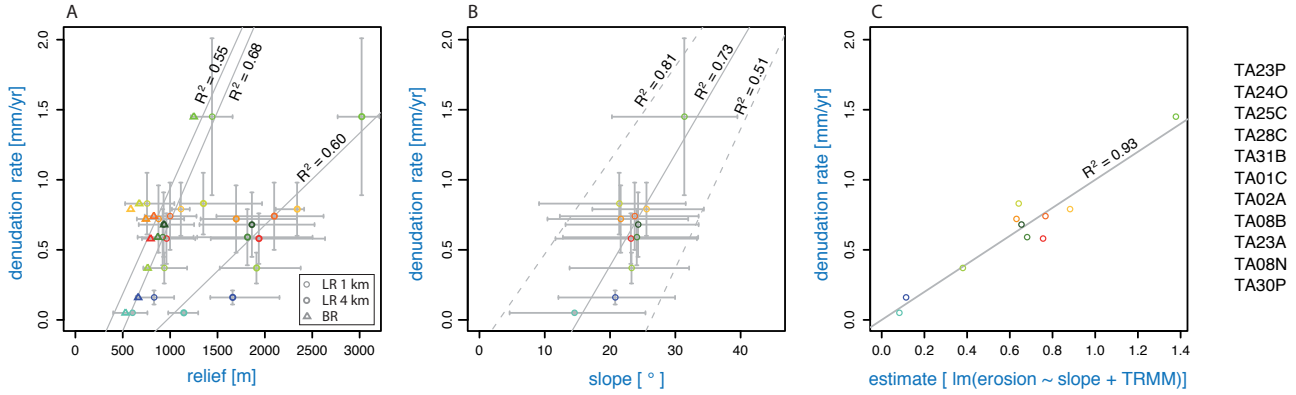

Figure 4. Robust linear regression analyses for denudation rates and the basin parameters relief **(a)**, slope **(b)** and slope combined with precipitation **(c)**. Panel **(a)**: scale-dependent relief calculation. (BR: basin relief representing the difference between the 0.75 and 0.25 quartiles of basin altitudes; LR: local relief determining the altitude range within moving windows of 1 km and 4 km. Values of each basin represent the median and the range between the 0.75 and 0.25 quartiles). Panel **(b)**: basin slopes representing the median of slopes within individual basins. Slope variations are shown according to the 0.25 and 0.75 quartiles. Panel **(c)**: multiple linear regression revealed highest correlation of denudation rates with the 0.75 quartiles of basin slope and TRMM-based precipitation (lm: linear model used for multiple linear regression analyses). Solid lines show the robust linear regression for median values, dashed lines that of respective quartiles. R^2 gives the coefficient of determination.

increasing nuclide concentration and averaging time, respectively.

However, the estimated T_{ave} means that variations in the absolute extent of glaciated areas are possible. T_{ave} is largely longer than the period covered by available MODIS data on permanent snow and ice cover (MCD12Q1, Strahler et al., 1999, data set for the year 2010) and mostly too short to be resolved by glacial chronologies at the Pamir Plateau. We assume persistent climatic circulations with overall dry conditions during the last 10^2 yr to 10^3 yr and an only slightly more extensive snow and ice cover compared to our chosen reference, the MODIS data for the year 2010.

Another point to consider in terms of timescales is the nuclide build-up during the transport of grains from the source rock to the sampled site. Robust cosmogenic nuclide-derived denudation rates require short grain travel times through the sampled basin when compared to T_{ave} (Granger et al., 1996; von Blanckenburg, 2005; Dunai, 2010). A significant nuclide build-up would result in a downstream increase in ^{10}Be concentrations (Schaller et al., 2001). Such increasing nuclide concentrations are not indicated for sampled basins along the Panj. Concentrated discharge during the melting season and also the generally high slope angles (0.75 quartiles of 25–40°), especially in marginal downstream basin sections, may be responsible for the annual sediment transported over long distances. Only valleys in the plateau-related basins contain significant sediment fills that witness relatively long storage periods. Nevertheless, this is in agreement with determined denudation rates.

Centennial- to millennial-scale ^{10}Be-based denudation rates in tectonically active landscapes such as the Pamir can be dependent on the magnitude-frequency distribution of mass wasting (see, e.g., Wolman and Miller, 1960; Korup et al., 2010; Korup, 2012; Lupker et al., 2012). High-magnitude events deliver sediments to river channels with a low temporal frequency, and the effects of their stochastic

occurrences are likely already captured at decadal time intervals (Wolman and Miller, 1960; Korup, 2012). The very low abundance of remnants of such events in the study area (e.g. Lake Yashilkul upstream of the Gunt River) indicates their minor relevance in the Pamir region.

On the 10^6-year timescale, Stübner et al. (2013) estimated syn- to post-tectonic erosion rates of 0.3–0.5 mm yr^{-1} for the Shakhdara Dome in the southern Pamir and 0.1–0.3 mm yr^{-1} between the Shakhdara and Alichur Dome. These geometrically constrained, long-term estimates agree with the cosmogenic nuclide-based denudation rates of the same area. The higher rates fit the marginal conditions of the Gunt Basin, while the lower rates agree with the conditions in the inner southern Pamir (Shakhdara Basin). The indication of persistent low erosion over timescales from 10^4 to 10^6 yr suggests a long-term steady state on the plateau of the Pamir. The higher rates of ~ 0.7 mm yr^{-1} and up to ~ 1.5 mm yr^{-1} in most other basins at the Pamir margins delineate areas undergoing adjustment to uplift or base-level drop on a millennial scale. The high rates roughly compare to the up to 2.0 mm yr^{-1} of erosion inferred by Carrapa et al. (2014), who associate the intense erosion with persistent feedbacks between exhumation and pronounced precipitation in the western Pamir. Erosion rates from river load gauging are not available yet but may greatly differ from the ^{10}Be-based rates because they resolve (below) decadal variations on smaller scales. Consequently, such short-term data are, for example, more sensitive to low-frequency, high-magnitude events and hillslope–river-channel connectivity.

5.2 Spatial variations in denudation rates

The basin-wide denudation rates represent average estimates of the upstream areas. They may be biased in tectonically active landscapes, in which certain basin sections deliver disproportionally high amounts of sediments to the river channels, for example in the form of landslides (see, e.g., Granger et al., 1996; von Blanckenburg, 2005; Dunai, 2010). Most sampled basins are large enough to average the effects of single sediment sources, differences in the erodibility and quartz abundance of rock types. However, the sediment release from individual geomorphic units is certainly not uniform. Hence, small-scale in situ data are needed to resolve the erosional domains within the basins and refine their sediment contribution to the river channels.

In particular, the sediment delivery from snow- and ice-covered areas requires attention. There is currently no ideal way to deal with such entirely shielded areas of a basin. We excluded areas based on the permanent snow and ice cover (MODIS MCD12Q1, Strahler et al., 1999, data set for the year 2010) to derive production rates. They represent the basin sections exposed to the cosmic ray flux that produces ^{10}Be in situ in quartz grains.

However, the snow- and ice-covered areas deliver sediments that likely were completely shielded before (glacio-)fluvial transport. Their negligible ^{10}Be concentrations do not scale with the rate of denudation and dilute the ^{10}Be concentrations in the river channel sediments. Calculating the denudation rates using production rates representative of the non-snow- and ice-shielded areas of a basin (Fig. 4a) has several consequences. The excluded areas comprise the highest altitudes of a basin. Their exclusion lowers the production rates. But the lower production rates do not necessarily compensate for the amount of sediment exported from the snow- and ice-covered areas and may be insufficient, especially in the case of large quantities of glacial sediments in the sampled material.

Grains carried by glaciofluvial streams dilute the CN (cosmogenic nuclide) concentration with zero-CN grains that mimic instant erosion independent of the actual rate below the glacier. The effect on the total basin-wide denudation rate depends on the efficiency of glaciers to erode. But the efficiency of glacial processes and their influence on denudation is highly debated (see, e.g., Norton et al., 2010; Godard et al., 2012). The portion of grain exported from the excluded snow- and ice-covered areas is still unknown for the sampled basins. Further small-scale data of sediment yields may resolve the influences from snow- and ice-covered areas on denudation rates in the Pamir and refine their absolute magnitudes. Nonetheless, analyses of annual sediment yields do not indicate a significant relationship with meteorological factors such as temperature and glaciated areas (E. Pohl and R. Gloaguen, personal communication, 2015). The remobilisation of sediments from moraines is possible, but such glacial deposits are older than the time span captured by our data and are mainly found at the Pamir Plateau, where denudation is minimal. Their contribution to river sediments thus indicates marginal influence.

The relative abundance of glaciers seems to cause no systematic effects in the basins we studied as the percentage of snow- and ice-covered areas did not correlate with denudation rates.

The denudation rates of basins along the Panj vary only slightly from the Pamir average of ~ 0.64 mm yr^{-1}, without any clear trend from smaller to larger basins (Fig. 3). In contrast, the studied tributaries reveal strong spatial variations in denudation. The major tributary basins indicate increasing denudation to the northwest. This coincides with the decoupling of the east–west elongation basins from plateau-related basin sections (cf. TA02A). The slope-weighted approach allows us to infer denudation rates also for the marginal basin sections of the Gunt (TA31B and TA30P) and Bartang (TA01C and TA08N) rivers. Results support the delineation of very low denudation (about 0.05–0.16 mm yr^{-1}) in plateau-related areas and higher rates (about 0.54–1.45 mm yr^{-1}) in marginal (sub-)basins. The northwestward increase in denudation rates is also present when looking only at the marginal basins sections.

Overall, the ^{10}Be-based basin-wide denudation rates are 10 times lower than reported OSL-based incision rates along

the Panj. The incision rates cover the last major deglaciation period but indicate persistent rates over the last 26 kyr. The variations in magnitude suggest a dominant control from local factors (Fuchs et al., 2014). The discrepancy in rates indicates that the basin-wide denudation is not adjusted to the intense lowering of the local base levels at the Pamir margins, induced by the fluvial incision of the Panj. Despite the difference in absolute magnitude, the spatial pattern is consistent with fluvial incision along the Panj River profile and variations in denudation rates of westward draining (sub)basins (Fig. 5).

Both process rates have lower values in southern Panj basins (denudation: $0.58 \pm 0.18\,\mathrm{mm\,yr^{-1}}$; incision: 2–3 $\mathrm{mm\,yr^{-1}}$) and abruptly increase (denudation: $0.74 \pm 0.24\,\mathrm{mm\,yr^{-1}}$; incision: 7–10 $\mathrm{mm\,yr^{-1}}$) where the Panj turns to the north, cutting across the Shakhdara Dome (Fig. 5; Fuchs et al., 2013, 2014).

The slope-weighted estimates (ISHs and ISHn) highlight the local change in denudation from $0.46 \pm 0.15\,\mathrm{mm\,yr^{-1}}$ to $0.89 \pm 0.28\,\mathrm{mm\,yr^{-1}}$. The abrupt change corresponds to the local change in geomorphologic conditions that are illustrated by geomorphic parameters such as valley shape ratios (VSR), Hack indices and riverbed convexity (Fig. 5). The lower denudation rate of $0.37 \pm 0.11\,\mathrm{mm\,yr^{-1}}$ for the entire Gunt Basin (TA31B) coincides with lower incision rates determined north of the confluence with the Gunt River, where the Panj develops a more graded river profile (Fig. 5). Further north, average denudation rates of the Bartang (TA01C) and Vanj basins (TA02A) increase from 0.83 to 1.45 $\mathrm{mm\,yr^{-1}}$. This increase to the highest rates is not resolved in OSL-based incision rates. The fluvial incision varies at a rather moderate level (between 4 and 6 $\mathrm{mm\,yr^{-1}}$) that is better comparable to the Pamir-wide average incision (5–6 $\mathrm{mm\,yr^{-1}}$) and, on the relative scale, also to the average denudation rate of $\sim 0.64\,\mathrm{mm\,yr^{-1}}$. The decoupling of both trends may be related to the already large Panj Basin and thus less sensitive to signals recorded by smaller tributary basins.

The magnitude of denudation is comparable with rates determined across the steep escarpment of the Himalaya (see, e.g., Godard et al., 2010; Andermann et al., 2012; Burbank et al., 2012; Lupker et al., 2012; Scherler et al., 2014), although conditions are different in the Pamir. The monsoon-controlled southern flank of the Himalaya receives precipitation of up to $4\,\mathrm{m\,yr^{-1}}$. Erosion rates exceed $2\,\mathrm{mm\,yr^{-1}}$ where intense orographic precipitation prevails, while rates decrease to $\sim 0.1\,\mathrm{mm\,yr^{-1}}$ in the northern rain shadow of the Higher Himalayan and Tibetan Plateau (see, e.g., Burbank et al., 2012). Gabet et al. (2008) found erosion, measured based on sediment flux in Nepal rivers, to correlate with average monsoon precipitation, with an R^2 of ~ 0.9. This corresponds to sediment flux that broadly scales with discharge. Suspended load data show sediment flux dependent on the magnitude-frequency distribution of rainfall such that sediment pulses require an initial minimum of precipitation (Andermann et al., 2012; Burbank et al., 2012). Andermann et al. (2012) emphasize the role of intense precipitation in direct runoff and sediment supply from hillslopes. The temperature-sensitive discharge in the highly elevated northern rain shadow modulates the relation between precipitation and sediment flux by shifting the peak discharge to the melting season. The hysteresis of sediment load and discharge suggests a supply-limited behaviour (Andermann et al., 2012; Burbank et al., 2012). Godard et al. (2014) describe a strong increase in denudation from 0.5–1 $\mathrm{mm\,yr^{-1}}$ in the Lesser Himalaya to 2–3 $\mathrm{mm\,yr^{-1}}$ in the Greater Himalaya despite relatively similar precipitation rates (R^2 of 0.13). They suggest denudation adapting fast to climatic changes and infer first-order control from large-scale tectonic uplift rates (R^2 of 0.78). Vice versa, the long-term tectonic uplift and erosion show the same uniform rates ($\sim 10^5$ years, based on thermochronology) across the Greater Himalaya despite a 5-fold increase in precipitation (Burbank et al., 2003). This agreement supports the hypothesis of a primary tectonic control on the topographic steepness and erosion. The decoupling from changes in precipitation indicates complex interactions within basins, such as between channel steepness and width, and concentrated sediment transport (Burbank et al., 2003; Scherler et al., 2014).

Of all the predictors we have looked at, steep slopes (0.75 quartiles) are also the primary factor controlling denudation in the Pamir (R^2 of 0.81). Low denudation rates of $< 0.2\,\mathrm{mm\,yr^{-1}}$ are linked to the high-elevation, low-relief inner-plateau areas. This areas of (very) slow topographic evolution basically comprise the uplifted Cenozoic domes of the southern, central and eastern Pamir and its wide, sediment-filled valleys. At the Pamir margins, rapid base-level lowering by the Panj facilitates steep slopes that in turn trigger high denudation rates. However, the rates of 0.54–1.45 $\mathrm{mm\,yr^{-1}}$ in marginal basins do not balance the intense fluvial incision. The discrepancy may relate to a possible fast base-level drop caused by river captures across the Pamir domes (Fuchs et al., 2013, 2014), while hillslopes are unable to adjust. The highest denudation rates coincide with the increased precipitation at the northwestern Pamir margin, where the discrepancy with fluvial incision decreases rates 3–5 times lower. The increased adjustment suggests complex links between denudation, slopes angles, precipitation and base-level lowering. Precipitation alone does not reveal any correlation with denudation rates (R^2 of < 0.1). Combined with the parameter slope, multiple linear regression analyses suggest that both parameters can explain most of the denudation variance (R^2 of 0.93). This multiple relation indicates that steep slopes are the important precondition for precipitation to become a relevant driver of denudation. In the overall semi-arid Pamir, our data suggest that precipitation only becomes a limiting factor in areas characterized by high denudation rates. Most basins receive precipitation mainly in winter in the form of snow. The accumulation of winter precipitation causes a temperature-sensitive and spatially focussed discharge during the melting season. The re-

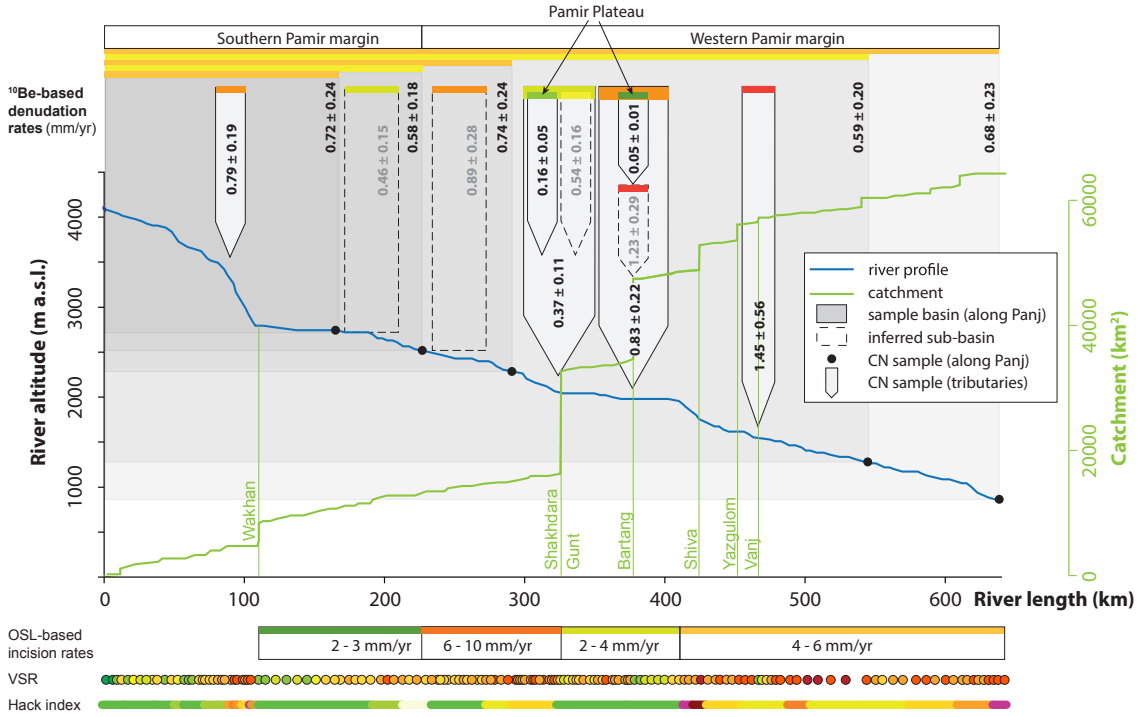

Figure 5. Variation in basin-averaged denudation rates and fluvial incision along the Panj (CN: cosmogenic nuclide; OSL: optically stimulated luminescence). The along-Panj samples (filled circles) represent ^{10}Be-based denudation rates that integrate over related upstream areas (grey shaded areas). Major tributaries and their sub-basins show local differences in denudation between marginal and plateau-related basin sections. The colour code illustrates the magnitude of denudation rates (green: low; red: high) and indicates the respective basin area. OSL-based incision rates, valley shape ratios (VSR) and Hack indices (Fuchs et al., 2013, 2014) along the Panj represent the pattern of fluvial incision that determines the lowering of local base levels at the Pamir margins.

sulting seasonal channelized discharge may control the sediment flux out of basins. The lowest discrepancy between hillslope processes and fluvial incision occurs in the northwestern Pamir, where precipitation is the highest. The highest discrepancy is found in the southern Pamir margins, where less precipitation is available for sediment transport on the hillslopes. Because of its disproportional intensity, fluvial incision induces persistent, steep slopes that in turn will sustain denudation. Denudation rates on the hillslopes might be limited by the availability of liquid water during most parts of the year (Pohl et al., 2015b).

6 Conclusions

The basin-wide denudation rates of $\sim 0.64\,\mathrm{mm\,yr^{-1}}$ for the entire Pamir highlight a rapid landscape evolution. This regional-scale denudation averages over very different geomorphological units of the orogen. Individual sub-basins of the major tributaries emphasize strong contrasts in denudation between the Pamir margins (0.54 to $1.45\,\mathrm{mm\,yr^{-1}}$) and the inner plateau (0.05 to $0.16\,\mathrm{mm\,yr^{-1}}$). The pattern of denudation reveals fast material removal at the Pamir margins that can be related to slope angles and a strong lowering of local base levels. Material resides for much longer periods on the Pamir Plateau, where large flat areas are evidence of the persistent local base level.

The prevalent steep slopes, in particular, affect denudation rates in the Pamir. The 0.75 quartiles of basin slope steepness explain about 80 % of the variance in denudation rates (R^2 of 0.81). Highest denudation rates at the Pamir margin coincide spatially with intense orographic precipitation delivered by the Westerlies. On the other hand, the entire data set of estimated denudation rates does not show any correlation with mean annual precipitation nor with snow and ice coverage (R^2 of <0.4). The multiple linear regression analyses (R^2 of 0.93) outline that the steepest slopes represent the most important precondition for an efficient denudation in the Pamir. However, sediment transport requires a minimum of precipitation. The water available for material transport is characterized by high spatiotemporal variations (Pohl et al., 2015b). Water discharge is largely controlled by the predominance of winter precipitation and its delayed, temperature-sensitive release during the melting season. The resulting peak discharge during spring and early summer provides the condition for an effective sediment mobilization out of basins (Pohl et al., 2015b) and, hence, contributes to high denudation, especially at the northwestern Pamir margin. The drier Pamir Plateau does not generate sufficient dis-

charge, and thus incision, which results in the prevalence of low slopes corresponding to low denudation rates. The wide, flat, sediment-filled valleys suggest that sediments remain for long periods of time on the plateau.

The magnitude of denudation is similar to rates determined across the south Himalayan escarpment and Tibetan Plateau (see, e.g., Godard et al., 2010; Andermann et al., 2012; Burbank et al., 2012; Lupker et al., 2012; Scherler et al., 2014), although both, climatic and tectonic conditions are different in the Pamir (see, e.g., Fuchs et al., 2013). In the semi-arid Pamir, incision clearly exceeds denudation. Basin-wide denudation rates do not balance the OSL-based incision rates of the Panj River, which are up to 10 times faster (Fuchs et al., 2014). This significant discrepancy implies a transient landscape. The limited coupling of denudation and incision has important implications for landscape evolution models and geohazard prediction (see, e.g., Gruber and Mergili, 2013). The dry conditions and low winter precipitation may limit the hillslope connectivity to river channels. Hillslopes that respond to base-level lowering only within the close vicinity of the river channel itself may intensify effects from hillslope length and channel network density. The strong incision and narrow radius of hillslope response suggest local relief steepening with an increasing risk of sudden slope failures and resulting debris flows or landslides. Additionally, the case of the Pamir shows not only the complex interplay of tectonic and climatic factors, but highlights especially the importance of internal feedbacks in an evolving drainage system, here in the form of river captures, that require an adequate implementation in landscape evolution models.

The Supplement related to this article is available online at doi:10.5194/esurf-3-423-2015-supplement.

Acknowledgements. We would like to thank the Department of Meteorology and Hydrology of Tajikistan for the support and organization during fieldwork in 2011. We are also grateful for the support of the DREAMS operator team facilitating AMS beam time, with special thanks to Shavkat Akhmadaliev, Stefan Pavetich and René Ziegenrücker. Furthermore, we thank the DFG for funding our research associated with the TIPAGE project (GI362/4-1). We used GMT (P. Wessel and W. H. F. Smith, New, improved version of the Generic Mapping Tools released, EOS Trans. AGU, 79, 579, 1998), QGIS (http://qgis.org/) and the R environment (http://www.r-project.org/) for most of the topographic data processing and the resulting figures. MODIS MCD12Q1 and ASTER GDEM data products were obtained through the online Data Pool at the NASA Land Processes Distributed Active Archive Center (LP DAAC), located at the US Geological Survey (USGS) Earth Resources Observation and Science (EROS) Center, Sioux Falls, South Dakota (https://lpdaac.usgs.gov/data_access).

Edited by: V. Vanacker

References

Abramowski, U., Bergau, A., Seebach, D., Zech, R., Glaser, B., Sosin, P., Kubik, P. W., and Zech, W.: Pleistocene glaciations of Central Asia: Results from ^{10}Be surface exposure ages of erratic boulders from the Pamir (Tajikistan), and the Alay–Turkestan range (Kyrgyzstan), Quaternary Sci. Rev., 25, 1080–1096, 2006.

Aizen, V.: Pamir glaciers, in: Encyclopedia of Snow, Ice and Glaciers. edited by: Sigh, V. P. and Singh, P., Haritashya, UK, 813–815, 2011.

Akhmadaliev, S., Heller, R., Hanf, D., Rugel, G., and Merchel, S.: The new 6 MV AMS-facility DREAMS at Dresden, Nucl. Instrum. Meth. B, 294, 5–10, 2013.

Andermann, C., Crave, A., Gloaguen, R., Davy, P., and Bonnet, S.: Connecting source and transport Suspended sediments in the Nepal Himalayas, Earth Planet. Sc. Lett., 351–352, 158–170, 2012.

Balco, G., Stone, J. O., Lifton, N. A., and Dunai, T. J.: A complete and easily accessible means of calculating surface exposure ages or erosion rates from ^{10}Be and ^{26}Al measurements, Quaternary Geochronology, 3, 174–195, 2008.

Bershaw, J., Garzione, C. N., Schoenbohm, L., Gehrels, G., and Tao, L.: Cenozoic evolution of the Pamir plateau based on stratigraphy, zircon provenance, and stable isotopes of foreland basin sediments at Oytag (Wuyitake) in the Tarim Basin (west China), J. Asian Earth Sci., 44, 136–148, 2012.

Bierman, P. R. and Steig, E. J.: Estimating rates of denudation using cosmogenic isotope abundances in sediment, Earth Surf. Proc. Land., 21, 125–139, 1996.

Bookhagen, B., Thiede, R. C., and Strecker, M. R.: Late Quaternary intensified monsoon phases control landscape evolution in the northwest Himalaya, Geology, 33, 149–152, 2005.

Brookfield, M. E.: Evolution of the great river systems of southern Asia during the Cenozoic India–Asia collision: Rivers draining north from the Pamir syntaxis, Geomorphology, 100, 296–311, 2008.

Brown, E. T., Edmond, J. M., Raisbeck, G. M., Yiou, F., Kurz, M. D., and Brook, E. J.: Examination of surface exposure ages of Antarctic moraines using in situ produced ^{10}Be and ^{26}Al, Geochim. Cosmochim. Acta, 55, 2269–2283, 1991.

Brown, E. T., Stallard, R. F., Larsen, M. C., Raisbeck, G. M., and Yiou, F.: Denudation rates determined from the accumulation of in situ-produced ^{10}Be in the Luquillo Experimental Forest, Puerto Rico, Earth Planet. Sc. Lett., 129, 193–202, 1995.

Burbank, D. W. and Anderson, R. S.: Tectonic geomorphology, Blackwell Science, Wiley, 288 pp., 2000.

Burbank, D. W., Blythe, A. E., Putkonen, J., Pratt-Sitaula, B., Gabet, E., Oskin, M., Barros, A., and Ojha, T. P.: Decoupling of erosion and precipitation in the Himalayas, Nature, 426, 652–655, 2003.

Burbank, D. W., Bookhagen, B., Gabet, E. J., and Putkonen, J.: Modern climate and erosion in the Himalaya, Comptes rendus – Geoscience, 344, 610–626, 2012.

Burtman, V. S. and Molnar, P.: Geological and physical evidence for deep subduction of continental crust beneath the Pamir, GSA Special Papers, 281, 1–76, 1993.

Carrapa, B., Shazanee Mustapha, F., Cosca, M., Gehrels, G., Schoenbohm, L. M., Sobel, E. R., DeCelles, P. G., Russell, J., and Goodman, P.: Multisystem dating of modern river detritus

from Tajikistan and China: Implications for crustal evolution and exhumation of the Pamir, Lithosphere, 6, 443–455, 2014.

Champagnac, J.-D., Schlunegger, F., Norton, K., von Blanckenburg, F., Abbühl, L. M., and Schwab, M.: Erosion-driven uplift of the modern Central Alps, Tectonophysics, 474, 236–249, 2009.

Codilean, A. T.: Calculation of the cosmogenic nuclide production topographic shielding scaling factor for large areas using DEMs, Earth Surf. Proc. Land., 31, 785–794, 2006.

Cowgill, E.: Cenozoic right-slip faulting along the eastern margin of the Pamir salient, northwestern China, Geol. Soc. Am. Bull., 122, 145–161, 2010.

Ducea, M. N., Lutkov, V., Minaev, V., Hacker, B. R., Ratschbacher, L., Luffi, P., Schwab, M., Gehrels, G. E., McWilliams, M., Vervoort, J., and Metcalf, J.: Building the Pamirs: The view from the underside, Geology, 31, 849–852, 2003.

Dunai, T.: Cosmogenic Nuclides: Principles, Concepts and Applications in the Earth Surface Sciences, Cambridge University Press, Cambridge, 198 pp., 2010.

Fan, G., Nil, J. F., and Wallace, T. C.: Active tectonics of the Pamir and Karakorum, J. Geophys. Res., 99, 7131–7160, 1994.

Fuchs, M. C., Gloaguen, R., and Pohl, E.: Tectonic and climatic forcing on the Panj river system during the Quaternary, Int. J. Earth Sci., 102, 1985–2003, 2013.

Fuchs, M. C., Gloaguen, R., Krbetschek, M. R., and Szulc, A.: Rates of river incision across the main tectonic units of the Pamir identified using optically stimulated luminescence dating of fluvial terraces, Geomorphology, 216, 79–92, 2014.

Gabet, E., Burbank, D. W., Pratt-Sitaula, B., Putkonen, J., and Bookhagen, B.: Modern erosion rates in the High Himalayas of Nepal, Earth Planet. Sc. Lett., 267, 482–494, 2008.

Gardelle, J., Berthier, E., Arnaud, Y., and Kääb, A.: Region-wide glacier mass balances over the Pamir-Karakoram-Himalaya during 1999–2011, The Cryosphere, 7, 1263–1286, doi:10.5194/tc-7-1263-2013, 2013.

Garzanti, E., Vezzoli, G., Andò, S., Lavé, J., Attal, M., France-Lanord, C., and DeCelles, P.: Quantifying sand provenance and erosion (Marsyandi River, Nepal Himalaya), Earth Planet. Sc. Lett., 258, 500–515, 2007.

Godard, V., Lavé, J., Carcaillet, J., Cattin, R., Bourlès, D., and Zhu, J.: Spatial distribution of denudation in Eastern Tibet and regressive erosion of plateau margins, Tectonophysics, 491, 253–274, 2010.

Godard, V., Burbank, D. W., Bourlès, D. L., Bookhagen, B., Braucher, R., and Fisher, G. B.: Impact of glacial erosion on ^{10}Be concentrations in fluvial sediments of the Marsyandi catchment, central Nepal, J. Geophys. Res., 117, F03013, doi:10.1029/2011JF002230, 2012.

Godard, V., Bourlès, D. L., Spinabella, F., Burbank, D. W., Bookhagen, B., Fisher, G. B., Moulin, A., and Leanni, L.: Dominance of tectonics over climate in Himalayan denudation, Geology, 42, 243–246, 2014.

Granger, D. E., Kirchner, J. W., and Finkel, R.: Spatial averaged long-term erosion rates measured from in situ-produced cosmogenic nuclides in alluvial sediment, J. Geol., 104, 249–257, 1996.

Gruber, F. E. and Mergili, M.: Regional-scale analysis of high-mountain multi-hazard and risk indicators in the Pamir (Tajikistan) with GRASS GIS, Nat. Hazards Earth Syst. Sci., 13, 2779–2796, doi:10.5194/nhess-13-2779-2013, 2013.

Herber, L. J.: Separation of feldspar from quartz by flotation, Am. Mineral., 54, 1212–1215, 1969.

Huffman, G. J., Adler, R. F., Arkin, P., Chang, A., Ferraro, R., Gruber, A., Janowiak, J., McNab, A., Rudolf, B., and Schneider, U.: The Global Precipitation Climatology Project (GPCP) Combined Precipitation Dataset, B. Am. Meteorol. Soc., 78, 5–20, 1997.

Huffman, G. J., Bolvin, D. T., Nelkin, E. J., Wolff, D. B., Adler, R. F., Gu, G., Hong, Y., Bowman, K. P., and Stocker, E. F.: The TRMM Multisatellite Precipitation Analysis (TMPA): Quasi-Global, Multiyear, Combined-Sensor Precipitation Estimates at Fine Scales, J. Hydrometeorol., 8, 38–55, 2007.

Huntington, K. W., Blythe, A. E., and Hodges, K. V.: Climate change and Late Pliocene acceleration of erosion in the Himalaya, Earth Planet. Sc. Lett., 252, 107–118, 2006.

Ischuk, A., Bendick, R., Rybin, A., Molnar, P., Khan, S. F., Kuzikov, S., Mohadjer, S., Saydullaev, U., Ilyasova, Z., Schelochkov, G., and Zubovich, A. V.: Kinematics of the Pamir and Hindu Kush regions from GPS geodesy, J. Geophys. Res.-Sol. Ea., 118, 2408–2416, 2013.

Korschinek, G., Bergmaier, A., Faestermann, T., Gerstmann, U. C., Knie, K., Rugel, G., Wallner, A., Dillmann, I., Dollinger, G., von Gostomski, C. L., Kossert, K., Maiti, M., Poutivtsev, M., and Remmert, A.: A new value for the half-life of ^{10}Be by Heavy-Ion Elastic Recoil Detection and liquid scintillation counting, Nucl. Instrum. Meth. B, 268, 187–191, 2010.

Korup, O.: Earth's portfolio of extreme sediment transport events, Earth-Sci. Rev., 112, 115–125, 2012.

Korup, O., Densmore, A. L., and Schlunegger, F.: The role of landslides in mountain range evolution, Geomorphology, 120, 77–90, 2010.

Koulakov, I. and Sobolev, S. V.: A tomographic image of Indian lithosphere break-off beneath the Pamir-Hindukush region, Geophys. J. Int., 164, 425–440, 2006.

Lal, D.: Cosmic ray labeling of erosion surfaces: in situ nuclide production rates and erosion models, Earth Planet. Sc. Lett., 104, 424–439, 1991.

Lupker, M., Blard, P.-H., Lavé, J., France-Lanord, C., Leanni, L., Puchol, N., Charreau, J., and Bourlès, D.: ^{10}Be-derived Himalayan denudation rates and sediment budgets in the Ganga basin, Earth Planet. Sc. Lett., 333–334, 146–156, 2012.

Merchel, S. and Herpers, U.: An update on radiochemical separation techniques for the determination of long-lived radionuclides via accelerator mass spectrometry, Radiochim. Acta, 84, 215–219, 1999.

Merchel, S., Arnold, M., Aumaître, G., Benedetti, L., Bourlès, D. L., Braucher, R., Alfimov, V., Freeman, S. P. H. T., Steier, P., and Wallner, A.: Towards more precise ^{10}Be and ^{36}Cl data from measurements at the 10^{-14} level: Influence of sample preparation, Nucl. Instrum. Meth. B, 266, 4921–4926, 2008.

Merchel, S., Bremser, W., Akhmadaliev, S., Arnold, M., Aumaître, G., Bourlès, D. L., Braucher, R., Caffee, M., Christl, M., Fifield, L. K., Finkel, R. C., Freeman, S. P. H. T., Ruiz-Gómez, A., Kubik, P. W., Martschini, M., Rood, D. H., Tims, S. G., Wallner, A., Wilcken, K. M., and Xu, S.: Quality assurance in accelerator mass spectrometry: Results from an international round-robin exercise for ^{10}Be, Nucl. Instrum. Meth. B, 289, 68–73, 2012.

Mohadjer, S., Bendick, R., Ischuk, A., Kuzikov, S., Kostuk, A., Saydullaev, U., Lodi, S., Kakar, D. M., Wasy, A., Khan, M. A., Molnar, P., Bilham, R., and Zubovich, A. V.: Parti-

tioning of India-Eurasia convergence in the Pamir-Hindu Kush from GPS measurements, Geophys. Res. Lett., 37, L041737, doi:10.1029/2009GL041737, 2010.

Molnar, P. and England, P.: Late Cenozoic uplift of mountain ranges and global climate change: chicken or egg?, Nature, 346, 29–34, 1990.

Montgomery, D. R. and Brandon, M. T.: Topographic controls on erosion rates in tectonically active mountain ranges, Earth Planet. Sc. Lett., 201, 481–489, 2002.

Nishiizumi, K., Imamura, M., Caffee, M. W., Southon, J. R., Finkel, R. C., and McAninch, J.: Absolute calibration of ^{10}Be AMS standards, Nucl. Instrum. Meth. B, 258, 403–413, 2007.

Norton, K. P. and Vanacker, V.: Effects of terrain smoothing on topographic shielding correction factors for cosmogenic nuclide-derived estimates of basin-averaged denudation rates, Earth Surf. Proc. Land., 34, 145–154, 2009.

Norton, K. P., Abbuhl, L. M., and Schlunegger, F.: Glacial conditioning as an erosional driving force in the Central Alps, Geology, 38, 655–658, 2010.

Ouimet, W. B., Whipple, K. X., and Granger, D. E.: Beyond threshold hillslopes: Channel adjustment to base-level fall in tectonically active mountain ranges, Geology, 37, 579–582, 2009.

Pohl, E., Gloaguen, R., and Seiler, R.: Remote Sensing-Based Assessment of the Variability of Winter and Summer Precipitation in the Pamirs and Their Effects on Hydrology and Hazards Using Harmonic Time Series Analysis, Remote Sens., 7, 9727, doi:10.3390/rs70809727, 2015a.

Pohl, E., Knoche, M., Gloaguen, R., Andermann, C., and Krause, P.: Sensitivity analysis and implications for surface processes from a hydrological modelling approach in the Gunt catchment, high Pamir Mountains, Earth Surf. Dynam., 3, 333–362, doi:10.5194/esurf-3-333-2015, 2015b.

R Core Team: R: A Language and Environment for Statistical Computing, R Foundation for Statistical Computing, Vienna, Austria, http://www.R-project.org (last access: 7 November 2014), 2013.

Reigber, C., Michel, G. W., Galas, R., Angermann, D., Klotz, J., Chen, J. Y., Papschev, A., Arslanov, R., Tzurkov, V. E., and Ishanov, M. C.: New space geodetic constraints on the distribution of deformation in Central Asia, Earth Planet. Sc. Lett., 191, 157–165, 2001.

Robinson, A. C.: Geologic offsets across the northern Karakorum fault: Implications for its role and terrane correlations in the western Himalayan-Tibetan orogen, Earth Planet. Sc. Lett., 279, 123–130, 2009.

Röhringer, I., Zech, R., Abramowski, U., Sosin, P., Aldahan, A., Kubik, P. W., Zöller, L., and Zech, W.: The late Pleistocene glaciation in the Bogchigir Valleys (Pamir, Tajikistan) based on ^{10}Be surface exposure dating, Quaternary Res., 78, 590–597, 2012.

Schaller, M., von Blanckenburg, F., Hovius, N., and Kubik, P. W.: Large-scale erosion rates from in situ-produced cosmogenic nuclides in European river sediments, Earth Planet. Sc. Lett., 188, 441–458, 2001.

Scherler, D., Bookhagen, B., and Strecker, M. R.: Tectonic control on 10Be-derived erosion rates in the Garhwal Himalaya, India, J. Geophys. Res.-Earth, 119, 83–105, 2014.

Schmidt, J., Hacker, B. R., Ratschbacher, L., Stübner, K., Stearns, M., Kylander-Clark, A., Cottle, J. M., Alexander, A., Webb, G., Gehrels, G., and Minaev, V.: Cenozoic deep crust in the Pamir, Earth Planet. Sc. Lett., 312, 411–421, 2011.

Schneider, F. M., Yuan, X., Schurr, B., Mechie, J., Sippl, C., Haberland, C., Minaev, V., Oimahmadov, I., Gadoev, M., Radjabov, N., Abdybachaev, U., Orunbaev, S., and Negmatullaev, S.: Seismic imaging of subducting continental lower crust beneath the Pamir, Earth Planet. Sc. Lett., 375, 101–112, 2013.

Schwab, M., Ratschbacher, L., Siebel, W., McWilliams, M., Minaev, V., Lutkov, V., Chen, F., Stanek, K., Nelson, B., Frisch, W., and Wooden, J. L.: Assembly of the Pamirs: Age and origin of magmatic belts from the southern Tien Shan to the southern Pamirs and their relation to Tibet, Tectonics, 23, TC4002, 2004.

Sippl, C., Schurr, B., Yuan, X., Mechie, J., Schneider, F. M., Gadoev, M., Orunbaev, S., Oimahmadov, I., Haberland, C., Abdybachaev, U., Minaev, V., Negmatullaev, S., and Radjabov, N.: Geometry of the Pamir-Hindu Kush intermediate-depth earthquake zone from local seismic data, J. Geophys. Res.-Sol. Ea., 118, 1438–1457, 2013.

Stone, J. O.: Air pressure and cosmogenic isotope production, J. Geophys. Res.-Sol. Ea., 105, 23753–23759, 2000.

Strahler, A., Muchoney, D., Borak, J., Friedl, M., Gopal, S., Lambin, E., and Moody, A.: MODIS Land Cover Product Algorithm Theoretical Basis Document (ATBD) Version 5.0, 1–59, 1999.

Strecker, M. R., Frisch, W., Hamburger, M. W., Ratschbacher, L., Semiletkin, S., Zamoruyev, A., and Sturchio, N.: Quaternary deformation in the Eastern Pamirs, Tadzhikistan and Kyrgyzstan, Tectonics, 14, 1061–1079, 1995.

Stübner, K., Ratschbacher, L., Weise, C., Chow, J., Hofmann, J., Khan, J., Rutte, D., Sperner, B., Pfänder, J. A., Hacker, B. R., Dunkl, I., Tichomirowa, M., Stearns, M. A., Bahram, I., Gadoev, M., Gloaguen, R., Jonckheere, R., Kanaev, E., Minaev, V., Oimahmadoc, I., Rajabov, N., and Stanek, K. P.: The giant Shakhdara migmatitic gneiss dome, Pamir, India-Asia collision zone, 2. Timing of dome formation, Tectonics, 32, 1404–1431, 2013.

Trifonov, V. G.: Late Quaternary tectonic movements of western and central Asia, Geol. Soc. Am. Bull., 89, 1059–1072, 1978.

von Blanckenburg, F.: The control mechanisms of erosion and weathering at basin scale from cosmogenic nuclides in river sediment, Earth Planet. Sc. Lett., 237, 462–479, 2005.

Wolman, J. G. and Miller, J. P.: Magnitude and frequency of forces in geomorphic processes, J. Geol., 68, 54–74, 1960.

Zech, R., Abramowski, U., Glaser, B., Sosin, P., Kubik, P. W., and Zech, W.: Late Quaternary glacial and climate history of the Pamir Mountains derived from cosmogenic ^{10}Be exposure ages, Quaternary Res., 64, 212–220, 2005.